ACS APPLIED MATERIALS & INTERFACES
Research Article
www.acsami.org

Unusual Dealloying Effect in Gold/Copper Alloy Thin Films: The Role of Defects and Column Boundaries in the Formation of Nanoporous Gold

Abdel-Aziz El Mel,*[†] Farah Boukli-Hacene,[†] Leopoldo Molina-Luna,[‡] Nicolas Bouts,[†] Adrien Chauvin,[†] Damien Thiry,[†] Eric Gautron,[†] Nicolas Gautier,[†] and Pierre-Yves Tessier[†]

[†]Institut des Matériaux Jean Rouxel, IMN, Université de Nantes, CNRS, 2 rue de la Houssinière, B.P. 32229, 44322 Nantes cedex 3, France

[‡]Technische Universität Darmstadt, Department of Material- and Geosciences, Alarich-Weiss-Strasse 2, 64287 Darmstadt, Germany

Supporting Information

ABSTRACT: Understanding the dealloying mechanisms of gold-based alloy thin films resulting in the formation of nanoporous gold with a sponge-like structure is essential for the future design and integration of this novel class of material in practical devices. Here we report on the synthesis of nanoporous gold thin films using a free-corrosion approach in nitric acid applied to cosputtered Au−Cu thin films. A relationship is established between the as-grown Au−Cu film characteristics (i.e., composition, morphology, and structure) and the porosity of the sponge-like gold thin films. We further demonstrate that the dealloying approach can be applied to nonhomogenous Au−Cu alloy thin films consisting of periodic and alternate Au-rich/Au-poor nanolayers. In such a case, however, the dealloying process is found to be altered and unusual etching stages arise. Thanks to defects and column boundaries playing the role of channels, the nitric acid is found to quickly penetrate within the films and then laterally (i.e., parallel to the film surface) attacks the nanolayers rather than perpendicularly. As a consequence to this anisotropic etching, the Au-poor layers are etched preferentially and transform into Au pillars holding the Au-rich layers and preventing them against collapsing. A further exposure to nitric acid results in the collapsing of the Au-rich layers accompanied by a transition from a multilayered to a sponge-like structure. A scenario, supported by experimental observations, is further proposed to provide a detailed explanation of the fundamental mechanisms occurring during the dealloying process of films with a multilayered structure.

KEYWORDS: *nanoporous gold, dealloying, copper, thin films, cosputtering*

1. INTRODUCTION

Dealloying is an ancient alchemy technique used in the past in depletion gilding for the surface enrichment of jewelry and artifacts of karat gold alloys.[1−3] Both experimental and theoretical backgrounds of dealloying are very well documented in the literature.[2−4] Briefly, during such a corrosion process, one or more constituents of a solid solution alloy are selectively dissolved, leaving behind a sponge-like structure of the more noble element with a uniform and open porosity. According to the leaching conditions (e.g., time, temperature, etc.), the size, shape, and density of the nanopores can be tuned accurately. Dealloying can be performed either by an electrochemical approach or by a free corrosion process in highly corrosive electrolyte (e.g., nitric acid). Although electrochemical dealloying allows an accurate monitoring of the etching process, a huge predilection was shown for the free corrosion approach due to its simplicity.

Despite the long and rich history of dealloying, the first evidence for the presence of nanoporosity in dealloyed metal alloys was reported by Pickering and Swann in the 1960s while investigating the corrosion of gold alloys using transmission electron microscopy (TEM).[5] Today, the dealloying approach has become very popular and was employed to synthesize various nanoporous materials (e.g., Au, Pt, Pd, Cu, etc.) using different metal alloy precursors including Au−Ag,[4,6−26] Au−Cu,[27−31] Au−Al,[32,33] Au−Pd−Ag,[34] Pt−Cu,[35,36] Pt−Fe,[37] Cu−Mn,[38] and Pt−Al.[39] In addition to the integration of nanoporous materials in various modern technological applications such as optical sensors,[20,21,40] Li-ion batteries,[18] actuators,[41] and catalysis,[36,42] understanding the fundamental mechanisms occurring during the dealloying process was among the main objectives of the studies reported so far in the literature. The first attempt to explain the dealloying mechanism was reported in the pioneering work of Forty in the 1970s who explored the dealloying process of Au−Ag alloys in nitric acid.[2,43,44] On the basis of the TEM observation of Au-

Received: September 24, 2014
Accepted: January 6, 2015
Published: January 6, 2015

DOI: 10.1021/am5065816
ACS Appl. Mater. Interfaces 2015, 7, 2310−2321

rich islands and silver-rich channels formed during dealloying, Forty proposed a scenario explaining the generation of porosity in the Au−Ag alloy as a consequence to the dissolution of silver in the electrolyte followed by the self-assembly of gold atoms.[42] Using an atomistic model, Erlebacher et al. have further demonstrated that the formation of nanoporosity is due to an intrinsic dynamical pattern formation process occurring during dealloying as a consequence of a spinodal decomposition process taking place at the solid alloy−electrolyte interface.[2,45] Several experimental works have followed and validated the atomistic model proposed by Erlebacher et al. including *in situ* X-ray diffraction,[29,30,35] focused ion beam nanotomography,[39] transmission electron tomography,[14] scanning TEM coupled to electron energy loss spectroscopy,[12] and scanning tunneling microscopy.[31] According to these studies,[2,3] to obtain uniform nanoporous gold, the composition and the structure of the Au-based alloy precursor must satisfy several requirements: (i) First, to trigger the dissolution process, the content of the less noble metal within the alloy must be higher than the parting limit. The parting limit can be defined as the dealloying threshold for the dissolution of the less noble component from a homogeneous binary alloy.[3] The parting limit varies from an alloy to another: it is close to 60 at. % of Ag in the case of Au−Ag[2] and about 40 at. % of Cu in the case of Au−Cu.[27] (ii) In addition to its composition, the alloy must exhibit a homogeneous single phase, since the presence of any possible phase separation can alter the dealloying process and thus impact the final structure of the nanoporous Au skeleton.[3]

Today, the conversion chemistry of Au-based solid alloys into nanoporous Au has attained enough maturity to start concentrating the efforts on the integration of this promising class of materials in practical applications. In this context, the light is being currently shade on the development of approaches allowing a simple integration of nanoporous gold in microdevices. An elegant way to achieve this purpose is by using thin films technology which was found to be a successful choice for the development of various devices including solar cells[46] and solid-state microbatteries.[47] Several studies have shown that nanoporous Au thin films can be prepared by dealloying Au-based alloy precursor thin films.[27,28,48] However, in the case of Au−Cu, which is the system investigated in this work, the reports were limited only on the $AuCu_3$ phase and no detailed study on the impact of the composition of the Au−Cu alloy on the formation of nanoporous Au was reported.[27−31] Among the various methods that can be used to deposit the Au-based thin film alloy precursors stands magnetron cosputtering which is a simple but efficient approach allowing the characteristics (e.g., composition, structure, morphology) of thin films to be controlled precisely over a large scale. However, since magnetron sputtering is a cold plasma process during which the deposition of the material occurs far from the thermodynamic equilibrium, the deposited Au-based alloys may exhibit a non-homogeneous structure (e.g., coexistence of different phases) and morphology. In addition, the phase separation phenomenon occurring at the nanoscale can result in the formation of a heterogeneous material, such as nanocomposites[49] or multilayers,[50] instead of a homogeneous one. Thus, when using cosputtered Au-based alloy thin films as precursors for the synthesis of nanoporous gold, their intrinsic properties (e.g., homogeneity of the alloy and defects within, structure and morphology of the films) are expected to alter the dealloying process and thus impact the final porosity of the films. Here we report on the dealloying effect of Au−Cu alloy thin films deposited by the cosputtering process at low temperature (less than 100 °C). Compared to the method reported by Morrish et al.,[27] which consists of the annealing of Au/Cu stacked layers at high temperature to form the Au−Cu alloy, cosputtering allows synthesizing various Au−Cu alloy thin films with various compositions at low temperature not exceeding 100 °C. We explore the impact of the composition, the structure, and the morphology of the as-grown thin film precursors on the dissolution kinetics of Cu as well as on the final porosity and crystalline structure of the obtained porous Au thin films. Investigating the alteration of the dealloying process due to the non-homogeneous structure and morphology of the used alloy precursors plays a central role in our study. More precisely, we focus on the role of defects and column boundaries on the creation of nanoporosity and how they generate unusual intermediate etching stages during the dealloying process.

2. EXPERIMENTAL SECTION

2.1. Deposition of Au−Cu Alloy Thin Films and Dealloying. The Au−Cu films were deposited by DC cosputtering in pure argon plasma of Au (diameter, 50.8 mm; purity, 99.99%) and Cu (diameter, 76.2 mm; purity, 99.99%) targets in a cofocal geometry. The distance between the targets and the substrate was 130 mm. To ensure a homogeneous deposition over a large surface, the samples were rotated at a speed of 5 turns/min. Prior to each deposition, a 50 nm Cr adhesion layer was grown by magnetron sputtering followed by a 20 nm thick layer of pure Au allowing protecting the Cr layer against oxidation. The deposition of the Au−Cu films was then carried out at a pressure of 0.5 Pa without any intentional heating of the substrate. However, under such deposition conditions, the temperature of the substrate is expected to stay less than 100 °C. For all depositions, the base pressure was less than 4×10^{-5} Pa. To control the composition of the films, the electrical power applied to the Cu target was fixed to 300 W, whereas the one applied to the Au target was tuned. Three electrical powers applied to the Au target were selected, 50, 100, and 150 W, allowing growing films with 16, 24, and 34 at. % of Au, respectively. For the purpose of comparison, the thickness of all the films was fixed to about 400 nm. For the scanning electron microscopy (SEM) analysis, the films were grown on a silicon substrate, whereas for the X-ray diffraction (XRD) measurements the films were grown on a glass substrate to avoid any possible reflections originating from the substrate.

The dealloying of the Au−Cu films was carried out in 70% concentrated nitric acid (15.7 M) from Sigma-Aldrich at room temperature. When achieving the desired etching time, the samples are then immersed in deionized water for several minutes to stop the dealloying process and remove the residue of nitric acid. As a safety precaution, all the dealloying experiments were carried out inside a fume hood to avoid any possible exposure to nitrogen dioxide (NO_2) which is a reddish-brown toxic gas emitted as a consequence of the reaction between nitric acid and copper.

2.2. Characterization. Plan-view and cross-section scanning electron microscopy (XSEM) imaging was carried out on a JEOL JSM 7600 F microscope operating at 5 kV. For cross-section SEM observations, the samples were cleaved using a diamond tip. The chemical composition of the films was determined by energy dispersive X-ray spectroscopy (EDS) performed on a JEOL 5600 microscope operating at 15 kV. For scanning transmission electron microscopy (STEM), a Cs-probe corrected JEOL ARM-F operated at 200 kV and provided with a Shottky-FEG was used. Imaging was done using both bright field STEM and high angle annular dark field (HAADF) STEM modes. Spatially resolved energy-dispersive X-ray spectroscopy was done with a JEOL EDS-system JED-2300T system provided with a 50 mm^2 light-element-sensitive X-ray detector, a digital pulse processor for high-speed accumulation, and a Be double tilt holder. Dynamic signal maps were obtained for Au−M (2−2.3 keV) and Cu−K (7.8−8.1 keV) using a 0.3 keV energy window, a 70

Figure 1. Scheme of the two-step fabrication process of nanoporous gold thin films based on the deposition of Au−Cu alloy followed by wet etching in nitric acid.

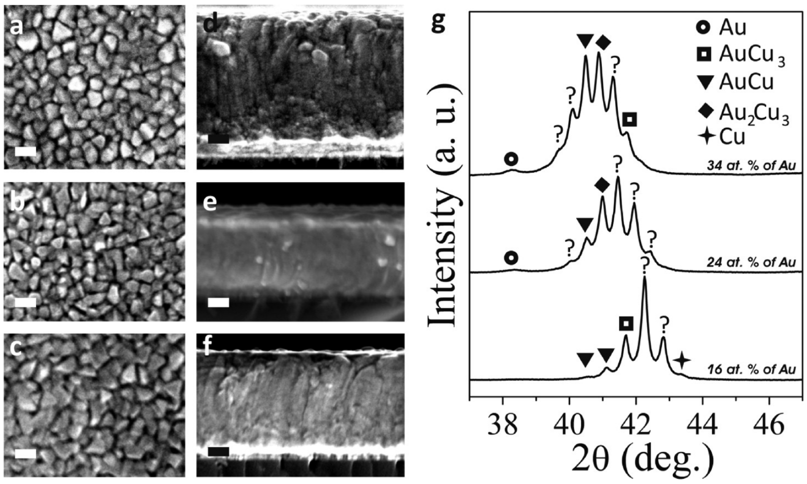

Figure 2. Plan-view (a−c) and cross-section (d−f) SEM micrographs of the as-grown Au−Cu thin films with a Au content of 16 at. % (a, d), 24 at. % (b, e), and 34 at. % (c, f). Scale bar: 100 nm. (g) X-ray diffraction patterns recorded on Au−Cu with different Au contents. The question marks in panel g represent the unidentified crystalline phases. The XRD patterns were indexed from the database: Au (JCPDS 03-065-2870), ordered tetragonal AuCu (JCPDS 00-025-1220), disordered orthorhomic AuCu (JCPDS 00-038-0741), $AuCu_3$ (JCPDS 03-065-3249), and Cu (JCPDS 00-004-0836).

μm condenser aperture, a pixel step of 2.1 nm, and a pixel time of 10 s. A hard X-ray aperture of 200 μm was inserted to avoid stray radiation. The data acquisition was done using Digital Micrograph (DM) software, and spatial drift correction was applied. Data analysis was performed with DM and ImageJ software. The STEM specimen was prepared by mechanical polishing followed by ion milling. For the structural analysis of the films, XRD measurements were carried out on a Siemens D5000 X-ray diffractometer in Bragg−Brentano θ−2θ geometry using the Cu Kα radiation as an incident beam.

3. RESULTS AND DISCUSSION

3.1. Au−Cu Alloy Precursors. The nanoporous Au thin films were prepared by a free corrosion approach in nitric acid applied at room temperature to Au−Cu thin film precursors deposited by magnetron cosputtering (Figure 1). Au−Cu films with different Au contents were selected for this study: 16, 24, and 34 at. % of Au. For the three types of samples, pyramidal grains were observed on the plan-view SEM micrographs (Figure 2a−c). While the films with 16 (Figure 2d) and 34 at. % (Figure 2f) show a columnar morphology, the one with 24 at. % of Au (Figure 2e) was found to be highly ductile during the cleavage before the XSEM observation and thus cannot be characterized properly. However, according to the structure zone model of elemental materials deposited by physical vapor deposition at low pressure and temperature, such films are expected to exhibit a columnar morphology, similarly to the two other conditions.[51]

The crystalline structure of the as-grown Au−Cu films was probed using XRD (Figure 2g). For films with 16 at. % of Au, one can identify three peaks located at 2θ values of 40.54, 41.12, and 41.70°, which correspond, respectively, to AuCu(111) with an ordered tetragonal structure, AuCu(120) with a disordered orthorhombic structure, and $AuCu_3$(111) with a cubic structure. A very weak peak at 43.31°, assigned to the (111) reflection of fcc Cu, indicates the presence of metallic copper in a very small amount in this type of films. Two peaks at 42.26 and 42.81° could not be assigned from the XRD database. For the films containing 24 at. % Au, three peaks located at 38.32, 40.51, and 40.93° are detected and can be assigned to the (111) reflection of fcc Au, the (111) reflection of tetragonal AuCu, and the (1111) reflection of orthorhombic Au_2Cu_3, respectively. For this condition, four peaks located at 40, 41.45, 41.94, and 42.44° could not be assigned on the basis of the XRD database. In the case of films with 34 at. % Au, the three peaks located at 38.32, 40.5, and 40.9°, identified previously in the case of the film with 24 at. % of Au, were also detected. In addition, a peak at 41.70°, which can be attributed to the (111) reflection of $AuCu_3$ with a cubic phase, was also detected. Three peaks located at about 39.7, 40.10, and 41.3° could not be identified using the XRD database.

As one can conclude, in the case of the three types of samples, the XRD analysis reveals peaks which are not listed in the XRD database. Despite an extensive search in the literature, we were unable to identify the crystalline phases to which the detected peaks can be attributed. Most probably, these peaks may originate from some crystalline nonstoichiometric Au_xCu_y phases present within the alloy. These phases may exhibit shifted peaks with respect to the stoichiometric ones. The presence of a local stress within the alloy due to the lattice mismatch between the different Au_xCu_y phases is also an additional reason amplifying the shift in position of the diffraction peaks. Since one Au_xCu_y phase may exhibit multiple diffraction peaks that can overlap with the ones originating from the other phases due to the shift in position, assigning these unindentified diffraction peaks based only on the experimental data is far from being obvious. A theoretical crystallographic simulation, which can be the subject of a forthcoming study, is required to clearly understand the unknown origins of these peaks.

3.2. Dealloying and Generation of Nanoporosity.

When placing copper in nitric acid, copper oxidizes to Cu^{2+} according to eq 1 and HNO_3 reduces into nitrogen dioxide gas:

$$Cu^0 \rightarrow Cu^{2+} + 2e^- \tag{1}$$

To monitor the dissolution kinetics of Cu upon immersion of the Au−Cu films in nitric acid, *ex situ* EDS was employed. Whatever the dealloying time, for all the experiments, no oxygen was detected by EDS, indicating that the samples are free of copper-based precipitations such as copper nitrate and copper oxide. Knowing the initial Cu content within the film ($\%Cu_{t0}$) as well as the one after a specific etching time ($\%Cu_t$) determined by EDS, one can easily calculate the fraction of Cu dissolved in nitric acid as follows:

$$\text{Dissolved Cu }(\%) = \frac{\%Cu_{t0} - \%Cu_t}{\%Cu_{t0}} \times 100 \tag{2}$$

For the three types of film (i.e., 16, 24, and 34 at. % of initial Au content) considered in this study, the dissolved amount of Cu in nitric acid increases as the dealloying process progresses in time (Figure 3). For films with an initial Au content of 16 at. %, Cu dissolves rapidly during the early stage of etching, since more than 60% of Cu is removed from the films during the first 30 s of exposure to nitric acid. This result reflects the very fast dissolution kinetics of Cu under such conditions. Between 5 and 60 min, the dissolution kinetics of Cu becomes much slower. Removing the entire Cu residue from the films, however, requires a very long dealloying time of up to 300 min. For films with initial Au content higher than 24 at. %, the dissolution kinetics of Cu is found to be much slower compared to the previous condition. In addition, an etching time of 300 min is found to be not sufficient to entirely remove the Cu residue from the films. The observed decrease in the dissolution kinetics is probably related to the local passivation of the surface of the alloy by Au clusters formed during the etching process as a consequence of the surface migration and coalescence of the less coordinated Au atoms.[2,3] This surface passivation effect is expected to become more important when the initial amount of Au within the alloy becomes higher.[2,3]

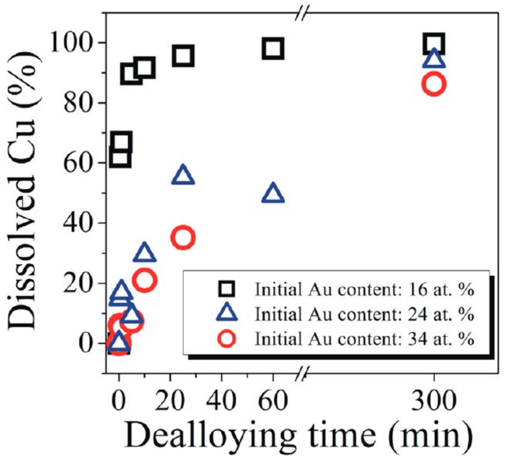

Figure 3. Evolution of the dissolved amount of Cu as a function of the dealloying time in nitric acid.

The morphological evolution of the films was monitored for different dealloying times using SEM (Figure 4). As expected, for all the films, the porosity becomes more important as the dealloying time is increased. For films with an initial Au content of 16 at. %, after 0.5 min of dealloying, very small pores and cracks appear on the surface. After 5 min of etching, these pores expand and become interconnected. The pore size becomes larger for an etching time of 25 min. The formation of a network of nested ligaments can be remarked after 60 min of dealloying. It can be noticed that increasing the dealloying time to 300 min results in the increase of the mean diameter of the formed ligaments. The films with an initial Au content of 24 at. % show a very similar morphological evolution with a reduced kinetics during the first 5 min. Interconnected ligaments form after 60 min of dealloying, and they become larger after 300 min of etching. While the first two conditions were very similar, the films with an initial Au content of 34 at. % show a different morphological evolution. Between 0.5 and 5 min of etching, the surface of the films is constituted of grains and no pores are identified. Compared to samples before etching (Figure 2c and f), the films look less dense and less homogeneous, meaning that the surface of the films was subjected to a very slow dissolution process. When reaching 25 min, nanopores start forming and they become larger with increasing dealloying time. Contrary to the films with initial Au contents of 16 and 24 at. %, for this condition, no ligaments were formed for longer dealloying durations.

To build a full picture of the formed three-dimensional nanoporosity, XSEM analyses were also performed (Figure 5). For films with an initial Au content of 16 at. %, after 0.5 min of etching in nitric acid, periodic and discontinuous layers form but can be hardly identified on the XSEM micrograph (Figure 5 and Figure S1, Supporting Information). For 5 min of dealloying, the formed layers disappear and the morphology of the film becomes granular. When reaching 25 min, the film becomes constituted of ligaments oriented perpendicularly to the substrate surface. The diameter of the formed ligaments increases as the dealloying time increases. A surprising evolution was observed in the case of films with an initial Au content of 24 at. %. For an etching time of 0.5 min, three thin layers form on the extreme surface of the film. Increasing the etching time to 5 min results in the formation of periodic nanolayers extended over the entire thickness of the film. In addition to the fact that under such conditions the multilayer structure is clearly visible, compared to the previous condition (i.e., 16 at. % of Au), the formation kinetics of such periodic nanolayers is much slower. Increasing the dealloying time to 25 min results in the extinction of the nanolayers and the resulting morphology consists of vertically oriented ligaments. The formed ligaments become thicker as the dealloying time increases. For a short etching time (up to 5 min), the film

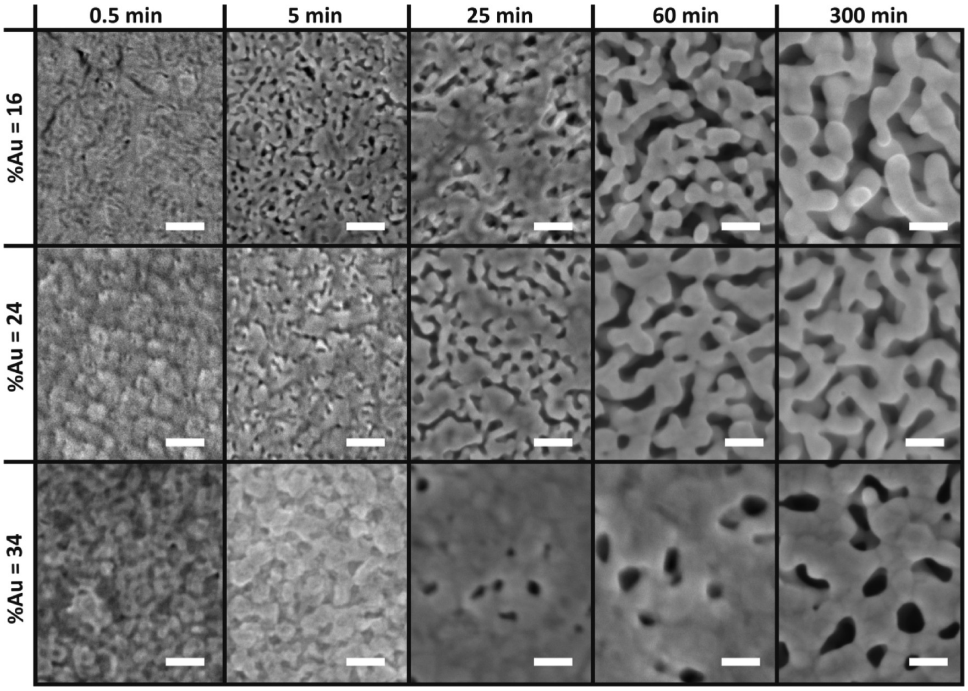

Figure 4. Plan-view SEM micrographs showing the impact of the dealloying time on the morphology of Au−Cu films with three different initial Au contents. Scale bar: 100 nm.

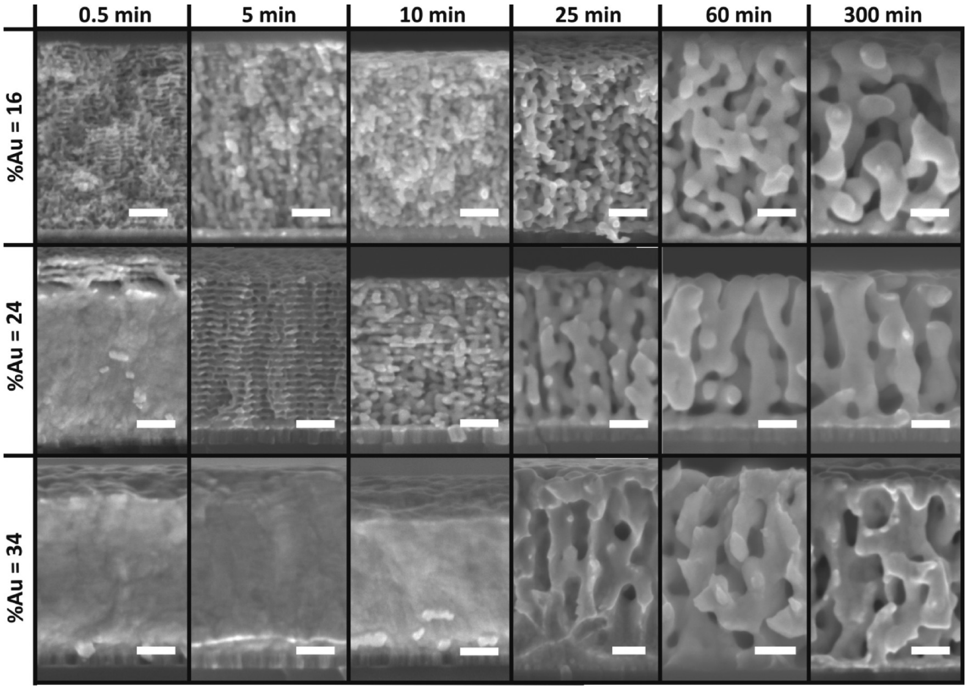

Figure 5. XSEM micrographs showing the impact of the dealloying time on the morphology of Au−Cu films with three different initial Au contents. Scale bar: 100 nm.

with 34 at. % of Au shows no remarkable morphological changes. For 25 min of dealloying, continuous pores form perpendicularly to the substrate surface. This morphology is very different from those observed for the previous conditions (i.e., 16 and 24 at. %) where ligaments were formed at this stage of etching. Furthermore, we can also notice that increasing the etching time leads to an increase in the diameter of the pores.

To compare the evolution of the pore size for the three types of samples as a function of the dealloying time, we conducted a statistical study on several plan-view SEM micrographs recorded on each sample (Figure 6a). For the three conditions, we can notice a very similar increase in the pore size from 10 to 75 nm as the dealloying time is increased. This result indicates that the lateral pore size is almost unaffected by the initial Au content within the films. On the other hand, we were not able to evaluate precisely the vertical size of the pores for the different conditions using the XSEM micrographs due to the formation of ligaments instead of pores under many etching

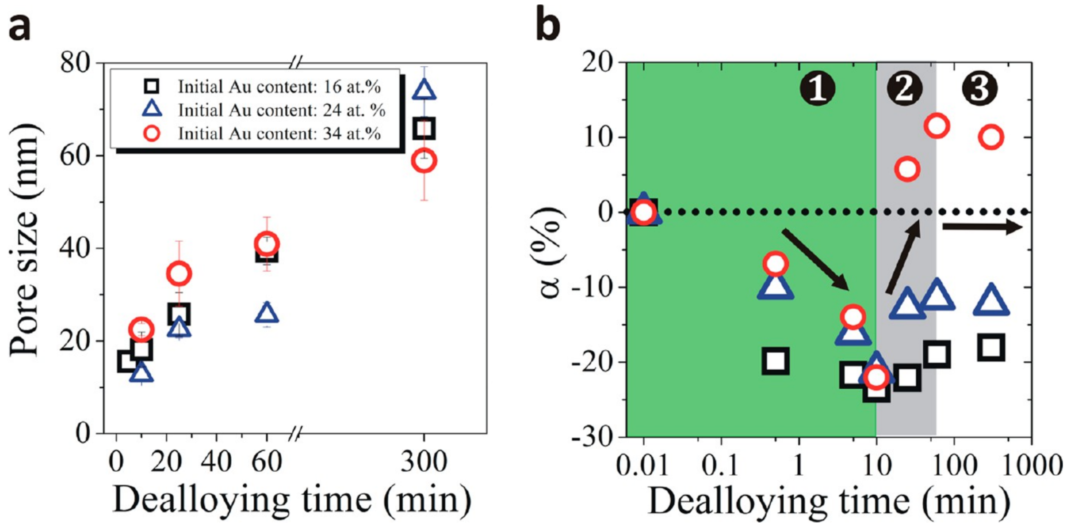

Figure 6. Chronological evolution of (a) the pore size and (b) the thickness of the films (in percent) as a function of the dealloying time for films with 16 (□), 24 (△), and 34 (○) at. % of initial Au content. A log scale is used for the *x* axis of panel b.

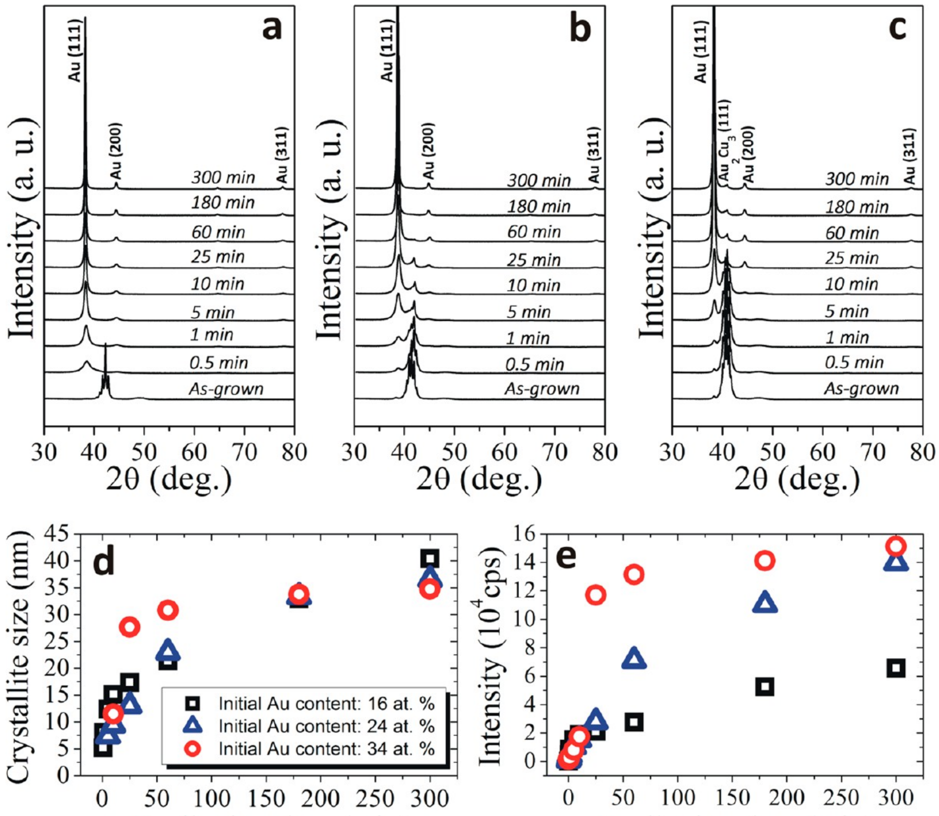

Figure 7. X-ray diffraction patterns recorded on Au−Cu films with an initial Au content of (a) 16 at. %, (b) 24 at. %, and (c) 34 at. %. (d) Evolution of the Au crystallite size and (e) the maximum of the Au(111) peak intensity as a function of the dealloying time.

conditions. However, we have remarked that, when the nanopores can be clearly identified (i.e., thin films with an initial Au content of 34 at. %), their vertical sizes are found to be larger than their lateral ones. Such shape elongation reflects the presence of a strong anisotropic etching taking place during the dealloying process along the vertical direction.

The evolution of the thickness of the films as a function of the dealloying time was also determined from the XSEM micrographs. A parameter α can be defined as follows:

$$\alpha\ (\%) = \frac{d_t - d_0}{d_0} \times 100 \tag{3}$$

Here, d_0 and d_t stand for the thickness of the films before and after an etching time t, respectively. The parameter α reflects the change in percent of the thickness after dealloying where a negative (positive) value represents a drop (increase) in thickness with respect to the thickness of the as-grown films (i.e., thickness before dealloying). For the three samples,

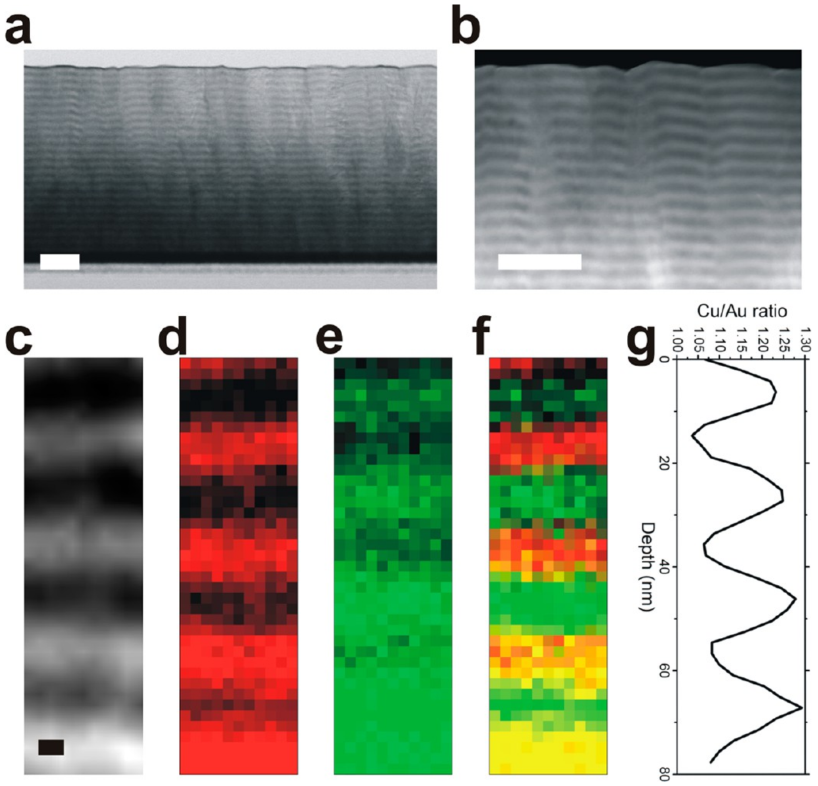

Figure 8. (a) Bright-field and (b) high angle annular dark field (HAADF) STEM micrographs recorded on an as-grown Au−Cu thin film with 24 at. % of Au. (c) Magnified HAADF micrograph showing the area analyzed by STEM-EDS. (d) Color coded Au−M EDS-dynamic map corresponding to 2−2.3 keV. (e) Color coded Cu−K EDS-dynamic map corresponding to 7.9−8.1 keV. (f) Overlaid RGB image of the Au−M and Cu−K EDS dynamic maps. (g) Cu/Au ratio corresponding to a line scan on the EDS mapping. White scale bar, 100 nm; black scale bar, 5 nm.

according to the evolution of α, three different regimes can be identified (Figure 6b). In the first regime, ranging between 0 and 10 min, α is negative and it decreases as the dealloying time is increased, indicating a decrease in thickness with respect to the initial thickness of the film. In the second regime between 10 and 60 min, α increases with the dealloying time. This means that the thickness of the films undergoes an increase after the drop in thickness observed in the first regime. It can be remarked that the increase of α in the second regime becomes more significant as increasing the initial Au content within the films. In the case of the films with an initial Au content of 16 and 24 at. %, although α increases in the second regime, its value stays negative, meaning that the thickness remains inferior to the one of the as-grown film. On the other hand, for the films with an initial Au content of 34 at. %, α increases until reaching positive values, indicating that, at this stage of dealloying, the thickness of the porous film becomes higher than the initial thickness before dealloying. When reaching 60 min, α enters in the third regime where it becomes almost constant for a further increase in the dealloying time. The stability in thickness can be correlated to the dissolution kinetics of Cu which becomes limited and slower within this range of etching time (see Figure 3).

3.3. Crystalline Structure of the Nanoporous Films. To follow the evolution of the crystalline phases forming during the dealloying process, *ex situ* XRD was carried out in a systematic manner on all the samples after each dealloying step. As it can be noticed in Figure 7a, for the sample with an initial Au content of 16 at. %, after 0.5 min of etching in nitric acid, the peaks assigned to the different Au−Cu alloys (i.e., $AuCu_3$, AuCu, Au_2Cu_3) disappear and only the peak of Au(111) is detected. A further increase in the dealloying time induces an increase in intensity of this peak, reflecting an increase in the overall quantity of the formed Au nanocrystallites exhibiting a preferential crystal orientation along the (111) axis. This result is consistent with the ones reported by Morrish et al., who also observed the same preferential orientation while studying the dealloying effect of the Au−Cu system.[27] The increase in intensity is accompanied by the appearance of a new peak at 44.38° which corresponds to the (200) reflection of fcc Au. After 25 min of dealloying, we can identify two other peaks at 64.54 and 77.52° which can be assigned to the (220) and (311) crystalline planes of fcc Au. For the sample with an initial Au content of 24 at. % (Figure 7b), a short etching time induces a change in peak intensity of Au(111) located at 38.18° and a decrease in intensity of all the peaks located between 40.02 and 42.44° previously assigned to the different phases of Au−Cu alloys. After 60 min of etching, the (200) and (220) peaks of fcc Au are also detected. In addition to these peaks, a peak assigned to the Au(311) is observed for an etching time between 180 and 300 min. For an initial Au content of 34 at. %, an increase in intensity of the Au(111) and an attenuation of the peaks located between 40.13 and 41.73°, attributed to the different phases of the Au−Cu alloys, can be noticed (Figure 7c). In the case of this sample, even for a long dealloying time of 300 min, a peak at 40.87°, corresponding to the Au_2Cu_3 phase, remains present.

On the basis of the XRD results, one can conclude that, as the initial Au content increases, the suppression of the Au−Cu alloy phases present within the as-grown films becomes harder. This is consistent with the EDS results presented previously which have shown that the dissolution kinetics of Cu decreases when increasing the initial Au content within the films. Since the Au(111) peak becomes sharper and more intense, it can also be concluded that the size and the amount of the Au crystallites formed during the dealloying process increase during dealloying. To support this conclusion, the Au crystallite size was evaluated using the Debye−Scherrer method applied to the Au(111) peak. As expected, for the three samples, the Au crystallite size is found to increase with the dealloying time (Figure 7d). The three used precursor alloys show very similar results in terms of data point values and trends. This is a direct proof that the initial compositions of the Au−Cu alloy do not impact the final crystallite size. This is probably related to the fact that the formation of the Au crystallite depends on the surface diffusivity of the Au adatoms at the solid alloy−electrolyte interface which is mainly influenced by the dealloying temperature.[7] The maximum of the Au(111) peak intensity is found to increase with increasing dealloying time, reflecting the increase of the volume of the Au crystallites oriented along the [111] axis and formed during etching (Figure 7e). We can also notice that, for a dealloying time higher than 25 min, the intensity becomes more important as the initial Au content is increased within the alloy precursor. This means that, as the initial Au content within the alloy precursor increases, the amount of the Au crystallites formed after a specific dealloying time becomes more important.

3.4. Periodic Nanolayers. To understand the formation of periodic nanolayers observed in the case of films with an initial Au content of 24 at. % and dealloyed for 5 min, it is important to know the intrinsic characteristics of the film precursor used. For this purpose, a structural investigation of the alloy precursor was carried out using STEM. The bright field STEM micrograph recorded on the film precursor reveals the presence of periodic nanolayers (20 nm in periodicity) with an alternate contrast (Figure 8a). Thus, the multilayered porous structure observed after 5 min of dealloying using XSEM is related to the intrinsic characteristic of the as-grown alloy precursor. It can also be remarked that the film has a columnar morphology where each column is formed of periodic nanolayers (Figure S2, Supporting Information). The HAADF-STEM imaging (Figure 8b), which is a technique strongly sensitive to compositional variation (*Z*-contrast image), demonstrates that the dark and bright layers have different chemical compositions: the dark layers are expected to be Au-poor (i.e., Cu-rich) and the bright ones are Au-rich (i.e., Cu-poor). This chemical variation is further confirmed on a set of nanolayers (Figure 8c) using STEM-EDS dynamic mapping (Figure 8d−f). The Cu/Au ratio is found to vary between 1 and 1.2 when going from a bright to a dark layer corresponding to a variation in the chemical composition of up to 20%. The origin of the multilayered structure is most probably related to the sample rotation applied during the cosputter deposition. One comes to such a conclusion due to the presence of a relationship between the number of formed layers and the one of rotations applied to the sample during deposition. Considering a deposition time of 5 min as well as a rotation speed of 5 turns/min, the number of rotations can be estimated to about 25 turns. If each rotation results in the formation of two nanolayers, one Au-rich (sample position close to the Au target) and another Au-poor (sample position close to the Cu target), the expected number of the formed layers is 50. The fact that this value is the same as the one deduced from the STEM micrograph of the as-grown Au−Cu film proves that the observed multilayered structure is an artifact originating from the rotation applied to the samples during deposition. To further support this conclusion, we have grown films at different rotation speeds (5, 2.5, 1, and 0 turns/min) while keeping the deposition time fixed to 5 min. As it can be seen in the XSEM micrographs (Figure 9), the morphology of these films dealloyed for 5 min evolves as a function of the rotation speed. While the number of the formed nanolayers decreases with decreasing rotation speed, their thickness is found to increase. Furthermore, the film grown in the static mode (i.e., without rotation) does not show the multilayered structure

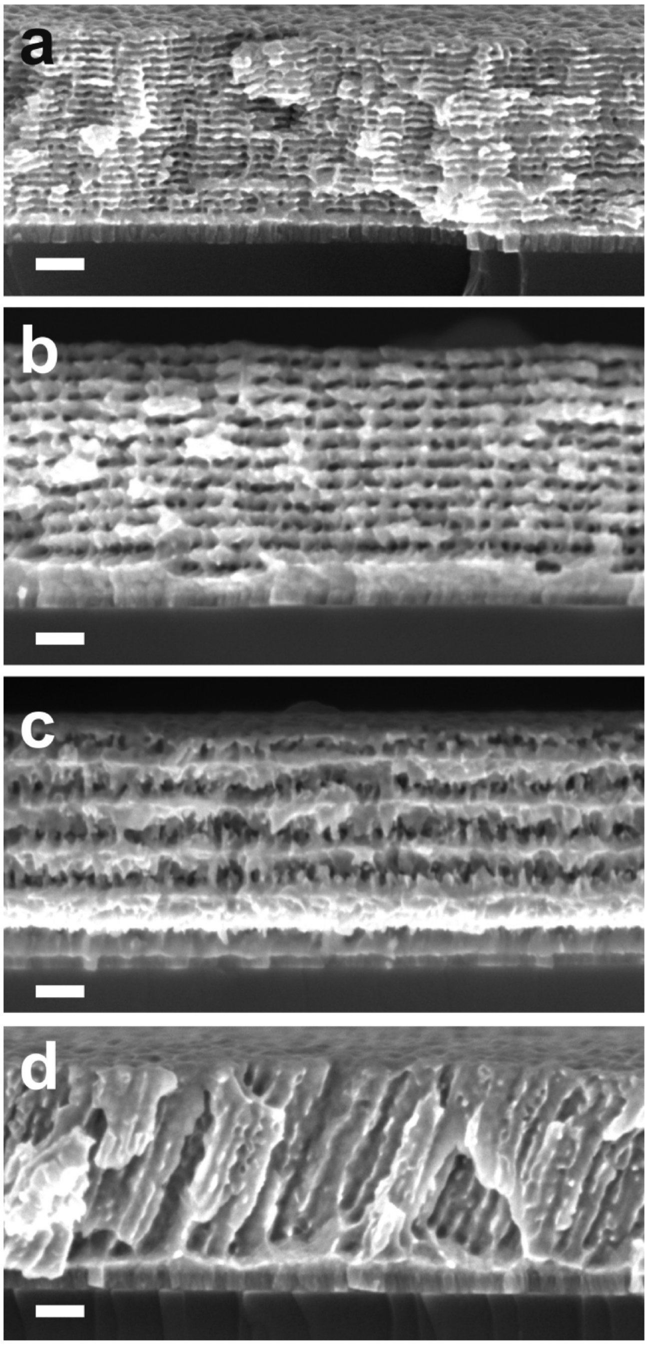

Figure 9. XSEM micrographs of Au−Cu films with an initial Au content of 24 at. % after dealloying for 5 min. For all the samples, the deposition time was fixed to 5 min and the rotation speed was varied: (a) 5 turns/min, (b) 2.5 turns/min, (c) 1 turn/min, and (d) 0 turns/min. Scale bar: 100 nm.

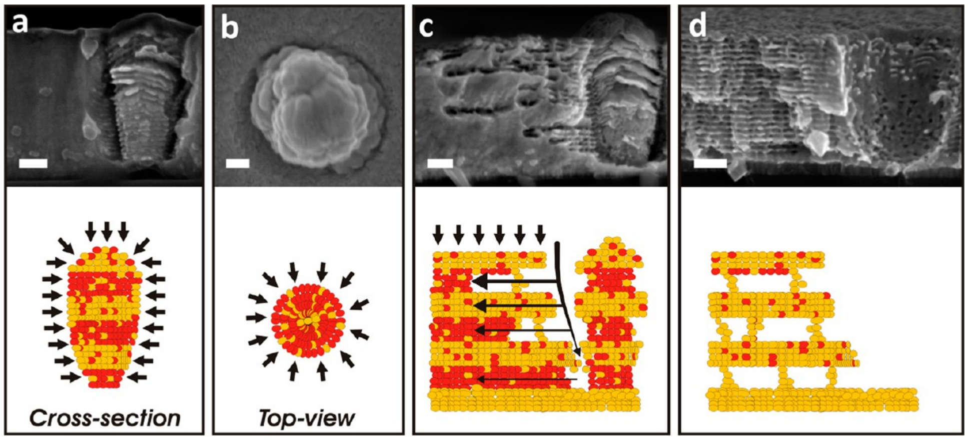

Figure 10. SEM micrographs and the corresponding schemes illustrating the lateral etching mechanism occurring near a column for different dealloying times: (a, b) 0.5 min, (c) 1 min, and (d) 5 min. The initial Au content of the used Au−Cu film precursor is 24 at. %. The black arrows used in the schemes illustrate the propagation paths of nitric acid, whereas the red and yellow color represents copper and gold, respectively. Scale bar: 100 nm.

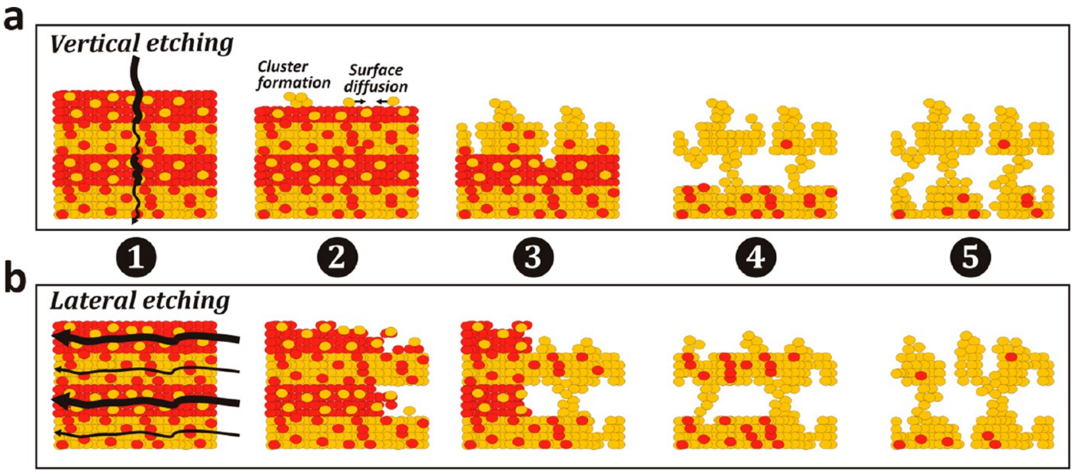

Figure 11. Two etching modes explaining the dealloying process of the multilayered Au−Cu thin films: (a) vertical and (b) lateral etching modes. The red and yellow color represents copper and gold, respectively.

observed previously (Figure 9d). This result supports our supposition explaining the formation of multilayers as a consequence of the sample rotation during the cosputter deposition.

While examining the films with such multilyared structure obtained after dealloying, we remarked that an anisotropic etching mechanism is taking place during dealloying due to defects (Figure 10). This type of defects was identified in the films before dealloying, and they can be described as columns separated from the rest of the film. The large gap present between the columns and the rest of the film plays the role of channels for the quick penetration of nitric acid. After 0.5 min of dealloying, while the column has already exhibited a multilayered structure over its entire body, an unpronounced multilayered structure appears over the walls of the film surrounding the column (Figure 10a). This result indicates that the etching process of the column is faster than the one of the walls of the film. This is probably related to the fact that a column is symmetrically surrounded by nitric acid in a three-dimensional manner (Figure 10b) which is expected to amplify the dissolution of Cu from the alloy. For 1 min of dealloying, one can clearly see the lateral propagation of nitric acid though the film occurring as a consequence to the penetration of nitric acid through the channels present around the column (Figure 10c). It can be seen that the lateral etching is faster close to the surface of the film and becomes slower when approaching the substrate. This effect can be related to the geometry of the channels, since they are broad at the region close to the surface of the film, allowing a large amount of nitric acid to penetrate quickly at the beginning, and then they become tighter when approaching the substrate which reduces both the propagation kinetics and the amount of nitric acid. As a consequence, the lateral etching rate close to the substrate is lower than the one close to the surface of the film. Increasing the dealloying time to 5 min results in the formation of multilayered structures over the entire thickness neighboring the column (Figure 10d). In the case of such samples, the columns were not observed by XSEM, supposing their probable delamination either during dealloying or during the cleavage of the sample for the XSEM observation.

On the basis of the previous observations, a scenario can be proposed to explain the transformation of the film's structure from multilayered to nanoporous while taking into account the role of defects and column boundaries (Figure 11). Contrary to homogeneous alloys, in the case of a multilayered structure, two etching modes of Cu occur simultaneously: (i) vertical (i.e., perpendicular to the substrate surface) (Figure 11a) and (ii) lateral (i.e., parallel to the substrate surface) (Figure 11b). In the first mode, a layer-by-layer etching process occurs, since nitric acid is considered to propagate perpendicularly to the surface through the bulk of the film transforming a layer after another from solid to porous (Figure 11a). This mode alone does not allow obtaining the nanolayered and porous structure observed previously after 5 min of dealloying, since the perpendicular propagation of nitric acid through the material requires the complete transformation of a layer after another from solid to nanoporous. In the second mode (Figure 11b), which is the dominant mode in the case of a multilayered structure, defects and column boundaries play a central role, since they act as "empty" channels for the fast penetration and spreading of nitric acid within the film. As a consequence, all the layers forming the film undergo a simultaneous lateral etching. Since the dissolution of Cu from an Au-poor alloy is faster than in the case of an Au-rich one, the Au-poor layers are almost completely etched before the Au-rich ones are even partially etched (Figure 11b (2 and 3)). The less-coordinated Au adatoms generated during dealloying of the Au-poor layers tend to diffuse and aggregate together, leading to the formation of pillars soldering together the Au-rich layers and preventing them against collapsing (Figure 11b (4)). It is important to mention here that the distance separating two adjacent pillars is about 70 nm (Figure S2d, Supporting Information), which is quite close to the mean diameter of the columns forming the films before dealloying (Figure S2b, Supporting Information). As the dealloying progresses in time, the Au-rich layers become also porous, resulting in the transformation of the multilayered structure into a nanoporous one (Figure 11b (5)). The collapsing of the multilayered structure due to the generation of strains during the corrosion process has also a non-negligible role in the transformation process of the multilayered structure into a nanoporous one.[34,35,52]

4. CONCLUSIONS

In conclusion, a two-step approach has been developed to fabricate nanoporous gold thin films with a sponge-like structure at low temperature not exceeding 100 °C. This approach is based on a free-corrosion process in nitric acid applied to cosputtered Au−Cu thin films. The dissolution kinetics of Cu during the dealloying process was found to decrease with increasing initial Au content within the films. By adjusting the initial composition of the Au−Cu film precursors as well as the dealloying time, the pore size can be tuned between 10 and 75 nm. In addition to the evolution of the pore size, the crystalline structure of the nanoporous Au films was also found to evolve as a function of the dealloying time: the size and the amount of the Au crystallites increase with increasing dealloying time.

We further demonstrate that the dealloying process can also be applied to nonhomogenous Au−Cu films consisting of periodic nanolayers alternately rich and poor in gold. The thickness and the number of the layers can be controlled by simply adjusting the rotation speed applied during the cosputter deposition of the Au−Cu films. In the case of such nonhomogenous Au−Cu films, the nitric acid was found to attack laterally (i.e., parallel to the film surface) the films rather than perpendicularly (i.e., perpendicular to the film surface). As a consequence, after 5 min of dealloying, the Au-poor layers were simultaneously etched preferentially and transformed into Au pillars holding the Au-rich layers and preventing them against collapsing. The lateral etching mechanism was related to the presence of defects (e.g., pinholes) and column boundaries in the films which act as channels promoting the propagation of nitric acid through the film. From a fundamental point of view, this result is of particular interest, since we demonstrated for the first time that, thanks to defects present within the alloy precursor, the fabrication of nanoporous gold using the dealloying process does not require a homogeneous precursor alloy.

■ ASSOCIATED CONTENT

Ⓢ Supporting Information

TEM characterization of Au−Cu thin films with 24 at. % of Au. SEM micrograph of Au−Cu thin film with 16 at. % of Au after dealloying for 0.5 min. This material is available free of charge via the Internet at http://pubs.acs.org.

■ AUTHOR INFORMATION

Corresponding Author

*E-mail: Abdelaziz.elmel@cnrs-imn.fr. Phone: +33 240376325. Fax: +33 240373995.

Notes

The authors declare no competing financial interest.

■ ACKNOWLEDGMENTS

The authors gratefully acknowledge F. Petitgas (IMN, Nantes) for his technical assistance on the cosputtering system and N. Stephant (Nantes University) and L. Nguyen (IMN, Nantes) for their technical assistance on SEM. The JEOL JEM ARM 200-F (S)TEM used in this work was partially funded by the German Research Foundation (DFG). The authors thank the "Région des Pays de la Loire (France)" for financial support through the "Post-doctorats internationaux" program.

■ ABBREVIATIONS

SEM, scanning electron microscopy
STEM, scanning transmission electron microscopy
XRD, X-ray diffraction
EDS, energy dispersive X-ray spectroscopy

■ REFERENCES

(1) Reti, L. Parting of Gold and Silver with Nitric Acid in a Page of the Codex Atlanticus of Leonardo Da Vinci. *Isis* **1965**, *56*, 307−319.

(2) Arne, W.; Biener, J.; Erlebacher, J.; Bäumer, M. *Nanoporous Gold: From an Ancient Technology to a High-Tech Material*; RSC: Cambridge, U.K., 2012.

(3) Xu, Q. *Nanoporous Materials: Synthesis and Applications*; CRC Press: Boca Raton, FL, 2013.

(4) Yu, H. D.; Zhang, Z.; Han, M. Y. Metal Corrosion for Nanofabrication. *Small* **2012**, *8*, 2621−2635.

(5) Pickering, H. W.; Swann, P. R. Electron Metallography of Chemical Attack Upon Some Alloys Susceptible to Stress Corrosion Cracking. *Corrosion* **1963**, *19*, 373t−389t.

(6) Ding, Y.; Kim, Y. J.; Erlebacher, J. Nanoporous Gold Leaf: "Ancient Technology"/Advanced Material. *Adv. Mater.* **2004**, *16*, 1897−1900.

(7) Qian, L. H.; Chen, M. W. Ultrafine Nanoporous Gold by Low-Temperature Dealloying and Kinetics of Nanopore Formation. *Appl. Phys. Lett.* **2007**, *91*, 083105.

(8) Dotzler, C. J.; Ingham, B.; Illy, B. N.; Wallwork, K.; Ryan, M. P.; Toney, M. F. in situ Observation of Strain Development and Porosity Evolution in Nanoporous Gold Foils. *Adv. Funct. Mater.* **2011**, *21*, 3938−3946.

(9) Laocharoensuk, R.; Sattayasamitsathit, S.; Burdick, J.; Kanatharana, P.; Thavarungkul, P.; Wang, J. Shape-Tailored Porous Gold Nanowires: From Nano Barbells to Nano Step-Cones. *ACS Nano* **2007**, *1*, 403−408.

(10) Erlebacher, J.; Sieradzki, K. Pattern Formation During Dealloying. *Scr. Mater.* **2003**, *49*, 991−996.

(11) Dursun, A.; Pugh, D. V.; Corcoran, S. G. Dealloying of Ag-Au Alloys in Halide-Containing Electrolytes: Affect on Critical Potential and Pore Size. *J. Electrochem. Soc.* **2003**, *150*, B355−B360.

(12) Fujita, T.; Tokunaga, T.; Zhang, L.; Li, D.; Chen, L.; Arai, S.; Yamamoto, Y.; Hirata, A.; Tanaka, N.; Ding, Y.; Chen, M. Atomic Observation of Catalysis-Induced Nanopore Coarsening of Nanoporous Gold. *Nano Lett.* **2014**, *14*, 1172−1177.

(13) Gu, X.; Xu, L.; Tian, F.; Ding, Y. Au-Ag Alloy Nanoporous Nanotubes. *Nano Res.* **2009**, *2*, 386−393.

(14) Fujita, T.; Qian, L. H.; Inoke, K.; Erlebacher, J.; Chen, M. W. Three-Dimensional Morphology of Nanoporous Gold. *Appl. Phys. Lett.* **2008**, *92*, 251902.

(15) Bok, H. M.; Shuford, K. L.; Kim, S.; Kim, S. K.; Park, S. Multiple Surface Plasmon Modes for a Colloidal Solution of Nanoporous Gold Nanorods and Their Comparison to Smooth Gold Nanorods. *Nano Lett.* **2008**, *8*, 2265−2270.

(16) Hakamada, M.; Mabuchi, M. Nanoporous Gold Prism Microassembly through a Self-Organizing Route. *Nano Lett.* **2006**, *6*, 882−885.

(17) Ji, C.; Searson, P. C. Fabrication of Nanoporous Gold Nanowires. *Appl. Phys. Lett.* **2002**, *81*, 4437−4439.

(18) Yu, Y.; Gu, L.; Lang, X.; Zhu, C.; Fujita, T.; Chen, M.; Maier, J. Li Storage in 3D Nanoporous Au-Supported Nanocrystalline Tin. *Adv. Mater.* **2011**, *23*, 2443−2447.

(19) Qi, Z.; Weissmüller, J. Hierarchical Nested-Network Nanostructure by Dealloying. *ACS Nano* **2013**, *7*, 5948−5954.

(20) Zhang, L.; Chang, H.; Hirata, A.; Wu, H.; Xue, Q. K.; Chen, M. Nanoporous Gold Based Optical Sensor for Sub-Ppt Detection of Mercury Ions. *ACS Nano* **2013**, *7*, 4595−4600.

(21) Zhang, L.; Lang, X.; Hirata, A.; Chen, M. Wrinkled Nanoporous Gold Films with Ultrahigh Surface-Enhanced Raman Scattering Enhancement. *ACS Nano* **2011**, *5*, 4407−4413.

(22) Garcia-Gradilla, V.; Sattayasamitsathit, S.; Soto, F.; Kuralay, F.; Yardımcı, C.; Wiitala, D.; Galarnyk, M.; Wang, J. Ultrasound-Propelled Nanoporous Gold Wire for Efficient Drug Loading and Release. *Small* **2014**, *10*, 4154−4159.

(23) Xue, Y.; Markmann, J.; Duan, H.; Weissmüller, J.; Huber, P. Switchable Imbibition in Nanoporous Gold. *Nat. Commun.* **2014**, *5*, 4237.

(24) Li, X.; Chen, Q.; McCue, I.; Snyder, J.; Crozier, P.; Erlebacher, J.; Sieradzki, K. Dealloying of Noble-Metal Alloy Nanoparticles. *Nano Lett.* **2014**, *14*, 2569−2577.

(25) Wan, D.; Xia, X.; Wang, Y.; Xia, Y. Robust Synthesis of Gold Cubic Nanoframes through a Combination of Galvanic Replacement, Gold Deposition, and Silver Dealloying. *Small* **2013**, *9*, 3111−3117.

(26) Chae, W. S.; Gough, D. V.; Ham, S. K.; Robinson, D. B.; Braun, P. V. Effect of Ordered Intermediate Porosity on Ion Transport in Hierarchically Nanoporous Electrodes. *ACS Appl. Mater. Interfaces* **2012**, *4*, 3973−3979.

(27) Morrish, R.; Dorame, K.; Muscat, A. J. Formation of Nanoporous Au by Dealloying AuCu Thin Films in HNO_3. *Scr. Mater.* **2011**, *64*, 856−859.

(28) Wi, J. S.; Park, J. H.; Tominaka, S.; Lee, J. Y. Enhanced Two-Photon Luminescence from Nanoporous Gold Capped with Micro-contact-Printed Salts. *Phys. Status Solidi RRL* **2014**, *8*, 52−55.

(29) Renner, F. U.; Stierle, A.; Dosch, H.; Kolb, D. M.; Lee, T. L.; Zegenhagen, J. in situ X-Ray Diffraction Study of the Initial Dealloying and Passivation of Cu_3Au (111) During Anodic Dissolution. *Phys. Rev. B* **2008**, *77*, 235433.

(30) Renner, F. U.; Stierle, A.; Dosch, H.; Kolb, D. M.; Lee, T. L.; Zegenhagen, J. Initial Corrosion Observed on the Atomic Scale. *Nature* **2006**, *439*, 707−710.

(31) Pareek, A.; Borodin, S.; Bashir, A.; Ankah, G. N.; Keil, P.; Eckstein, G. A.; Rohwerder, M.; Stratmann, M.; Gründer, Y.; Renner, F. U. Initiation and Inhibition of Dealloying of Single Crystalline Cu_3Au (111) Surfaces. *J. Am. Chem. Soc.* **2011**, *133*, 18264−18271.

(32) Zhang, Z.; Wang, Y.; Wang, Y.; Wang, X.; Qi, Z.; Ji, H.; Zhao, C. Formation of Ultrafine Nanoporous Gold Related to Surface Diffusion of Gold Adatoms During Dealloying of Al_2Au in an Alkaline Solution. *Scr. Mater.* **2010**, *62*, 137−140.

(33) Cortie, M. B.; Maaroof, A. I.; Smith, G. B. Electrochemical Capacitance of Mesoporous Gold. *Gold Bull.* **2005**, *38*, 14−22.

(34) Detsi, E.; Punzhin, S.; Rao, J.; Onck, P. R.; De Hosson, J. T. M. Enhanced Strain in Functional Nanoporous Gold with a Dual Microscopic Length Scale Structure. *ACS Nano* **2012**, *6*, 3734−3744.

(35) Yang, R.; Strasser, P.; Toney, M. F. Dealloying of Cu_3Pt (111) Studied by Surface X-Ray Scattering. *J. Phys. Chem. C* **2011**, *115*, 9074−9080.

(36) Ge, X.; Chen, L.; Kang, J.; Fujita, T.; Hirata, A.; Zhang, W.; Jiang, J.; Chen, M. A Core-Shell Nanoporous Pt-Cu Catalyst with Tunable Composition and High Catalytic Activity. *Adv. Funct. Mater.* **2013**, *23*, 4156−4162.

(37) Shui, J.-l.; Chen, C.; Li, J. C. M. Evolution of Nanoporous Pt−Fe Alloy Nanowires by Dealloying and Their Catalytic Property for Oxygen Reduction Reaction. *Adv. Funct. Mater.* **2011**, *21*, 3357−3362.

(38) Chen, L. Y.; Yu, J. S.; Fujita, T.; Chen, M. W. Nanoporous Copper with Tunable Nanoporosity for Sers Applications. *Adv. Funct. Mater.* **2009**, *19*, 1221−1226.

(39) Galinski, H.; Ryll, T.; Schlagenhauf, L.; Rechberger, F.; Ying, S.; Gauckler, L. J.; Mornaghini, F. C. F.; Ries, Y.; Spolenak, R.; Döbeli, M. Dealloying of Platinum-Aluminum Thin Films: Dynamics of Pattern Formation. *Phys. Rev. Lett.* **2011**, *107*, 225503.

(40) Feng, J.; Wu, J. Nanoporous Gold Channel with Attached DNA Nanolock for Drug Screening. *Small* **2012**, *8*, 3786−3790.

(41) Biener, J.; Wittstock, A.; Zepeda-Ruiz, L. A.; Biener, M. M.; Zielasek, V.; Kramer, D.; Viswanath, R. N.; Weissmuller, J.; Baumer, M.; Hamza, A. V. Surface-Chemistry-Driven Actuation in Nanoporous Gold. *Nat. Mater.* **2009**, *8*, 47−51.

(42) Wittstock, A.; Zielasek, V.; Biener, J.; Friend, C. M.; Bäumer, M. Nanoporous Gold Catalysts for Selective Gas-Phase Oxidative Coupling of Methanol at Low Temperature. *Science* **2010**, *327*, 319−322.

(43) Forty, A. J. Corrosion Micromorphology of Noble Metal Alloys and Depletion Gilding. *Nature* **1979**, *282*, 597−598.

(44) Forty, A. J. Micromorphological Studies of the Corrosion of Gold Alloys. *Gold Bull.* **1981**, *14*, 25−35.

(45) Erlebacher, J.; Aziz, M. J.; Karma, A.; Dimitrov, N.; Sieradzki, K. Evolution of Nanoporosity in Dealloying. *Nature* **2001**, *410*, 450−453.

(46) Buffière, M.; Harel, S.; Guillot-Deudon, C.; Arzel, L.; Barreau, N.; Kessler, J. Effect of the Chemical Composition of Co-Sputtered Zn(O,S) Buffer Layers on Cu(In,Ga)Se2 Solar Cell Performance. *Phys. Status Solidi A* **2014**, DOI: 10.1002/pssa.201431388.

(47) Etman, A. S.; Radisic, A.; Emara, M. M.; Huyghebaert, C.; Vereecken, P. M. Effect of Film Morphology on the Li Ion Intercalation Kinetics in Anodic Porous Manganese Dioxide Thin Films. *J. Phys. Chem. C* **2014**, *118*, 9889−9898.

(48) McCurry, D. A.; Kamundi, M.; Fayette, M.; Wafula, F.; Dimitrov, N. All Electrochemical Fabrication of a Platinized Nanoporous Au Thin-Film Catalyst. *ACS Appl. Mater. Interfaces* **2011**, *3*, 4459−4468.

(49) El Mel, A. A.; Bouts, N.; Grigore, E.; Gautron, E.; Granier, A.; Angleraud, B.; Tessier, P. Y. Shape Control of Nickel Nanostructures Incorporated in Amorphous Carbon Films: From Globular Nanoparticles toward Aligned Nanowires. *J. Appl. Phys.* **2012**, *111*, 114309.

(50) Abrasonis, G.; Kovács, G. J.; Ryves, L.; Krause, M.; Mücklich, A.; Munnik, F.; Oates, T. W. H.; Bilek, M. M. M.; Möller, W. Phase Separation in Carbon-Nickel Films During Hyperthermal Ion Deposition. *J. Appl. Phys.* **2009**, *105*, 083518.

(51) Petrov, I.; Barna, P. B.; Hultman, L.; Greene, J. E. Microstructural Evolution During Film Growth. *J. Vac. Sci. Technol., A* **2003**, *21*, S117−S128.

(52) Fujita, T.; Tokunaga, T.; Zhang, L.; Li, D.; Chen, L.; Arai, S.; Yamamoto, Y.; Hirata, A.; Tanaka, N.; Ding, Y.; Chen, M. Atomic Observation of Catalysis-Induced Nanopore Coarsening of Nanoporous Gold. *Nano Lett.* **2014**, *14*, 1172−1177.